Superconductivity in thin films of RuN

A. S. Ilin,* A. O. Strugova, I. A. Cohn, V. V. Pavlovskiy, and S. V. Zaitsev-Zotov†
Kotelnikov Institute of Radioengineering and Electronics of RAS, Mokhovaya 11, bld. 7, 125009 Moscow, Russia and HSE University, Physics Deparment, Myasnitskaya Ulitsa, 20, 101000 Moscow, Russia

A. V. Sadakov, O. A. Sobolevskiy, L. A. Morgun, V. P. Matrovitskii, and G. V. Rybalchenko
P. N. Lebedev Physical Institute, Russian Academy of Sciences, Leninskiy Prospekkt, 53, 119991 Moscow, Russia

(Received 5 March 2024; accepted 1 July 2024; published 9 July 2024)

Superconductivity has been found in RuN films obtained by reactive magnetron sputtering. This novel member of the metal nitride superconductors family has a critical temperature of the superconducting transition that varies depending on the substrate, ranging from 0.77 K to 1.29 K. The parameters of the crystal lattice of the superconducting films have been determined: The lattice is cubic with rhombohedral distortion along the normal to substrate surface with parameters $a = b = c = 4.559$ Å for RuN/SiO_2, $a = b = c = 4.536$ Å for RuN/Si, and $\alpha = \beta = \gamma = 87.96^\circ$ for both films. The upper critical magnetic field at zero temperature $H_{c2}(0) = 2.3$–4.1 T found by extrapolation our experimental data collected at $T \gtrapprox 0.8$ to zero temperature using the WHH model is near the upper paramagnetic limit. An s-wave single-band energy gap of $\Delta(0) = 0.19$ meV was revealed by self-field critical current experiment at temperatures down to 10 mK.

DOI: 10.1103/PhysRevMaterials.8.074801

I. INTRODUCTION

Transition metal nitrides have been attracting the interest of researchers for decades due to a wide variety of electronic properties [1]. Moreover, many of metal nitrides are superconductors with a relatively high critical transition temperature T_c, which turns out to be higher than the critical temperature of the initial transition metal elements [2]. The superconducting properties of niobium and titanium nitrides are best studied, and to a lesser extent nitrides of most other transition metals: zirconium, vanadium, hafnium, molybdenum, tungsten, tantalum, and rhenium. At the same time, due to the complexity of synthesis [3], the superconducting properties of nitrides of platinum group metals remain poorly understood.

RuN films can be obtained by various methods: laser ablation of ruthenium in a nitrogen atmosphere [4], reactive magnetron sputtering [5–9]. The material is characterised by a positive enthalpy of formation. As a result, it is not stable against heating and loses nitrogen when heated above 200 °C [6,9]. Consequently, no nitrogen is detected in films grown by reactive magnetron sputtering if the substrate temperature exceeds 100 °C [9]. NaCl-like structure was reported for films deposited by pulsed laser deposition [4] and ZnS-like structure for ones grown by magnetron sputtering [7,8].

To the best of our knowledge, there is no information on the superconductivity of RuN films in the literature. In this paper, we demonstrate the presence of superconductivity in RuN thin films and present the main characteristics obtained through various analysis: crystal structure using x-ray diffraction, elemental composition using energy-dispersive spectroscopy, energy structure using density functional theory, and superconducting state parameters derived from measurements of critical temperature and current, depending on the magnetic field.

II. FILM GROWTH, THEIR STRUCTURE, AND COMPOSITION

A. Film growth

RuN films were grown by reactive magnetron sputtering in a pure nitrogen atmosphere on substrates of various types: single-crystal silicon (Si), thermally oxidized single-crystal silicon (Si/SiO_2), and quartz glass (SiO_2). Film deposition was carried out in a VON ARDENNE LS 730S setup. The residual gas pressure in the chamber and the nitrogen pressure were $<10^{-7}$ and 6×10^{-3} mbar, respectively, at a discharge current of 70–80 mA. The typical film thickness was around 100 nm. The films under study were deposited at room temperature in a single technological cycle.

B. Film composition

Figure 1 shows the elemental composition of a RuN/Si film obtained by the energy-dispersive x-ray spectroscopy (EDS) at different electron energies. We see that EDS results depends on the e-beam energy. This dependence corresponds to a shift of the effective analysis area deeper into the substrate with the increase in e-beam energy (the substrate contribution at 20 keV is dominant) and temperature instability of the films observed around 200 °C [6,9]. The damage produced by the e-beam during collecting EDS data at large energies is clearly

*Present address: Department of Condensed Matter Physics, Weizmann Institute of Science, Rehovoth, Israel.
†Contact author: serzz@cplire.ru

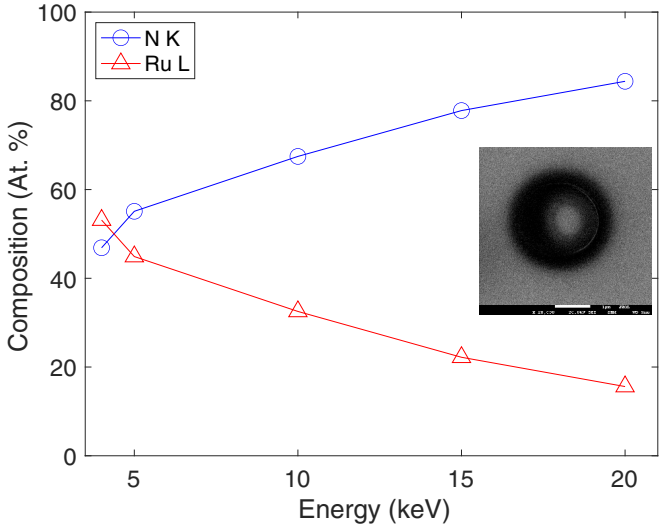

FIG. 1. EDS results obtained at different electron energies in RuN/Si film. The inset shows the area under analysis damaged by an electron beam with an energy of 20 keV. Scale mark is 1 μm.

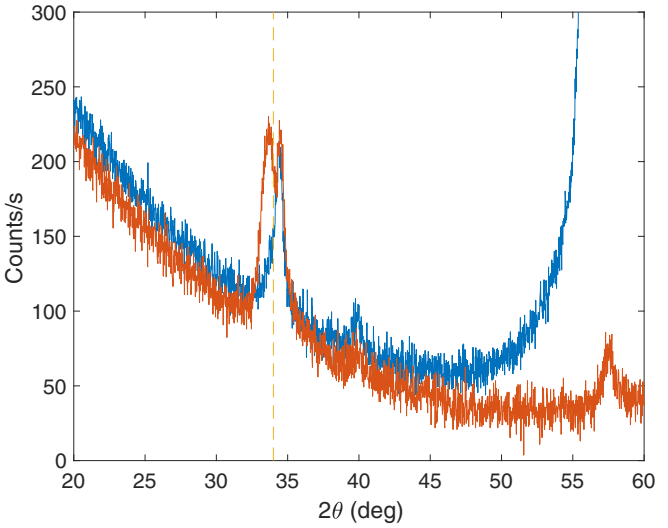

FIG. 2. Square scale x-ray diffraction patterns of a RuN sample on silicon obtained with a joint (2θ-ω) scan (blue) and with a fixed sample at an angle of $\omega = 3^\circ$ for 2θ scans (brick red).

seen in SEM images of the film surface (see inset in Fig. 1). The study of the elemental composition of the RuN films, the superconducting properties of which were investigated, carried out at an electron energy of 4 keV at which the substrate contribution does not exceed a few percent, gave 49.7%, 51,1%, and 50.6% of nitrogen and 50.3%, 48.9%, and 49.4% of ruthenium contents in the films grown on Si, oxidized Si, and SiO_2 substrates, respectively.

C. Films structure study

Structural studies were carried out on a Panalytical MRD diffractometer with a parabolic x-ray mirror as the primary monochromator and a third parallel analyzer. The samples were attached to a crystal holder made of single-crystal silicon to reduce the background.

Figure 2 shows x-ray diffraction patterns of a RuN film on a silicon substrate. The blue curve was obtained with a joint (2θ-ω) scan and the brick red with a fixed sample at an angle of $\omega = 3^\circ$ for 2θ scans. In the first case (blue), the reflecting planes are parallel to the substrate surface; in the second case, they are inclined to the surface (brick red). In the range of angles $2\theta \approx 34^\circ$ on the red curve, one of the two peaks disappears whereas the intensity of the peak at an angle of $2\theta \approx 40^\circ$ on the red curve increases. This indicates the existence of a preferential grain orientation parallel to the substrate surface. Unfortunately, an asymmetric silicon peak with a sharp increase in intensity partially overlaps with the red curve.

Figure 3 shows reflectometric curves of RuN films grown on different substrates. Ruthenium has a very high density (12.41 g/cm^3) compared to silicon (2.328 g/cm^3) or SiO_2 (2.64 g/cm^3). The greater the density, the higher the angle of total external reflection, the larger the difference between the densities of the layer and the substrate, and the greater the intensity of the satellites. In RuN/Si, the density is noticeably lower than in RuN/SiO_2 where the experimental reflectometric curve agrees with the calculated one (black). In addition, satellites are completely absent on the blue curve, and the decrease in intensity with increasing diffraction angle corresponds to a roughness of more than 10 nm. Reflectometry does not distinguish between the roughness of the upper surface and the diffusion smearing of the interface between the substrate and the layer. However, a decrease in density unambiguously testifies in favor of strong diffusion mixing of the composition of the epitaxial layer with the substrate.

Figure 4 shows a diffractogram of the RuN/SiO_2 film. It consists of two orders of the same reflection and clearly indicates a tendency for the material to orient itself with its basal plane along the surface of the substrate.

The rocking curve of the RuN layer on SiO_2 for the first reflection in the diffraction pattern is shown in the

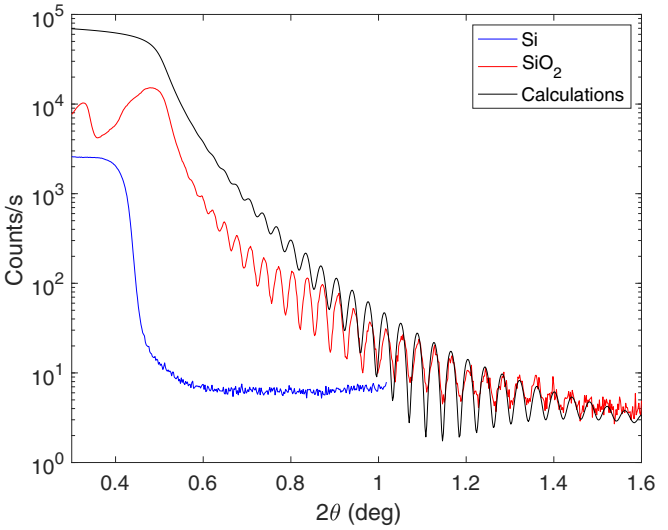

FIG. 3. Reflectometric curves of RuN films on silicon (blue), SiO_2 (red) substrates, and calculated curve (black) for a film with a thickness of 105 nm and a density of 7.5 g/cm^3 (black).

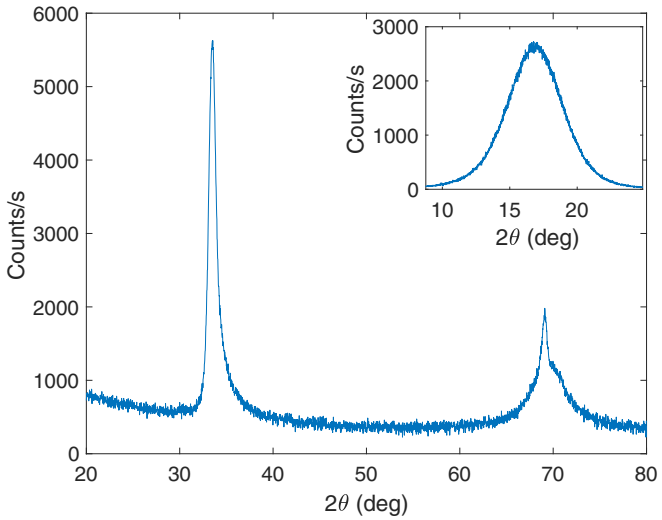

FIG. 4. Diffractogram of the RuN/SiO_2 film, consisting of two orders of the same reflection. The inset shows rocking curve of the RuN/SiO_2 film with half-width $\Delta\omega = 4.7^\circ$ for the first reflection in the diffraction pattern.

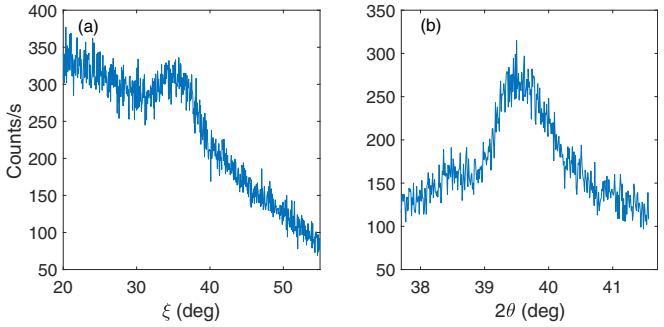

FIG. 5. (a) Results of ξ scanning when the sample plane deviates from the vertical with the angular position of the detector $2\theta = 56.8^\circ$. The maximum intensity of the reflection is at $\xi = 35.24^\circ$. (b) Results of $(2\theta\text{-}\theta)$ scanning on the asymmetric reflection of the RuN/SiO_2 film with the deviation of the sample plane by 35.24° from the vertical. By the angular position $2\theta = 56.764^\circ$ we find the value $d_5 = 1.6205$ Å. For RuN/Si film, $d_5 = 1.6015$ Å, which is noticeably smaller.

inset in Fig. 4. The maximum intensity coincides with the diffraction angle. This means that the epitaxial layer grows on an amorphous substrate with a basal plane nearly parallel to the substrate plane. In other words, it is an axial texture in which the normals to the basal plane of individual crystallites are approximately parallel, and the remaining normals to the asymmetric reflecting planes of the crystallites are evenly distributed circularly.

First of all, it is desirable to understand a crystal system of the RuN structure obtained and to calculate the unit-cell parameters. Ruthenium is better known in the hexagonal lattice $a = 2.724$ Å, $c = 4.332$ Å, but there is also a cubic variant $a = 3.83$ Å.

Let us start with the more common hexagonal structure, especially since there is a tendency for the layer to crystallize with the basal plane parallel to the substrate. If nitrogen does not change the hexagonal structure, then the first reflection perpendicular to the basal plane has the index (0002) allowed for the hexagonal structure and the value of the lattice parameter along the c axis is $c = 5.350$ Å. Then, the strong reflection with $d_3 = 2.612$ Å located near the first reflection can be the reflection $(10\bar{1}1)$ with $a_1 = 3.459$ Å, but the slope angle for it according to the crystallography formulas is $\phi_{(0001)/(10\bar{1}1)} = 60.76^\circ$ instead of the experimentally observed angle of 70.8°. For reflection $(11\bar{2}1)$ with $a_2 = 5.992$ Å $(0001)/(11\bar{2}1) = 60.75^\circ$. No other reflections of the hexagonal phase are suitable for explaining the observed experimental data.

If the layer lattice is cubic, then the first symmetric reflection has indices (111) and $a_{\text{cub}} = 4.633$ Å for $d_{(111)} = 2.675$ Å. In a cubic lattice, there is only one family of planes $(\bar{1}11)$, $(1\bar{1}1)$, and $(11\bar{1})$, forming an angle of 70.53° with the (111) plane, with the same interplanar spacing, and hence the same diffraction angle. But the experimental value of the interplanar distance for asymmetric reflections is smaller since the first pair of strong reflections on the diffraction pattern is bifurcated ($d_1 = 2.675$ Å, $d_3 = 2.612$ Å). A possible explanation is the following: The cubic lattice undergoes rhombohedral deformation (the cube lattice is elongated along one spatial diagonal [111], as a result of which the length of the lattice changes slightly, and the angles of the unit cell become less than 90°). Let us find the magnitude of the deformation of the corners from the bifurcation of the first two reflections. For $d_1 = 2.675$ Å and $d_3 = 2.612$ Å in terms of interplanar distances and the angle between them, they correspond to the lattice $a = b = c = 4.559$ Å, $\alpha = \beta = \gamma = 87.96^\circ$. The calculated angle of inclination of the three planes $(\bar{1}11)$, $(1\bar{1}1)$, and $(11\bar{1})$ to the (111) plane is 71.7°, which is close to the experimental value of 70.8°, taking into account the grain misorientation half-width of 4.7°. Let us now check this conclusion on other reflections.

The reflection in Figs. 5(a) and 5(b) with an angle of inclination to the basal plane of 35.24° and an angular position of $2\theta = 56.764^\circ$, $d_5 = 1.621$ Å can be identified as the reflection (022) with calculated $d_{(022)} = 1.624$ Å and an inclination angle of 38.7°, while for an undeformed cubic lattice the inclination angle is 35.26°. Little discrepancies can be associated with the layer defects, which concentration is noticeably greater in the layer on silicon. As a result, the maxima of the far reflection on the two substrates noticeably diverge ($2\theta_{\text{RuN/Si}} = 57.50^\circ$, $2\theta_{[\text{RuN/SiO2}} = 56.764^\circ$).

Thus, all RuN reflections observed on the diffractograms belong to a cubic lattice deformed along one spatial diagonal, with parameters $a = b = c = 4.559$ Å, $\alpha = \beta = \gamma = 87.96^\circ$ for RuN/SiO_2 film. Similarly, for RuN/Si film, the lattice parameters are $a = b = c = 4.536$ Å, $\alpha = \beta = \gamma = 87.96^\circ$.

III. NUMERICAL SIMULATION OF ELECTRONIC BAND STRUCTURE

The electronic band structure and Fermi surface calculations were performed using the Abinit package [10]. Conventional unit cell with the R3m:H rhombohedral symmetry [11] obtained above can be reduced to primitive unit cell with parameters $a = b = c = 3.2803$ Å and $\alpha = \beta = \gamma = 57.70^\circ$ (Fig. 6). Structure optimization was performed with

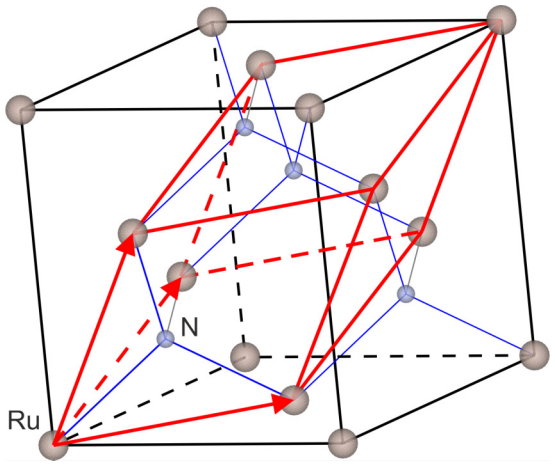

FIG. 6. Conventional (black) and primitive (red) unit cells of RuN.

full unit-cell optimization. Resulting lattice vector lengths were reduced by 0.05 Å (1.5%) and the angles were increased by 2.3° (4%). We used original lattice parameters obtained from the experiment for the electron band structure calculations.

The calculations were performed in the framework of density functional theory (DFT) and based on exchange-correlation functional with the Perdew-Burke-Ernzerhof (PBE) parametrization of the generalized gradient approximation (GGA). Spin-orbit coupling (SOC) was taken into account, and noncollinear full relativistic pseudopotentials were used because of the presence of rather heavy element Ru. An energy cutoff of 600 eV and k-point grid $31 \times 31 \times 31$ within the Monkhorst-Pack scheme were adopted for the Brillouin zone sampling.

Electron bands originating from Ru atom layers are affected by SOC, which follows from the results of RuN electronic band structure calculation (Fig. 7). SOC leads to the splitting of the electron dispersion curves, but some electronic states are kept degenerate along Γ–K, Γ–L, and Γ–X lines in the Brillouin zone. Fermi level ($E = 0$ in Fig. 7) crosses

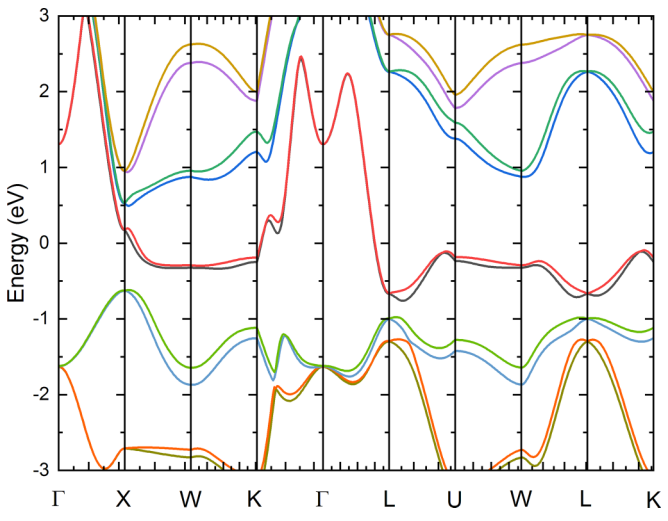

FIG. 7. RuN band structure.

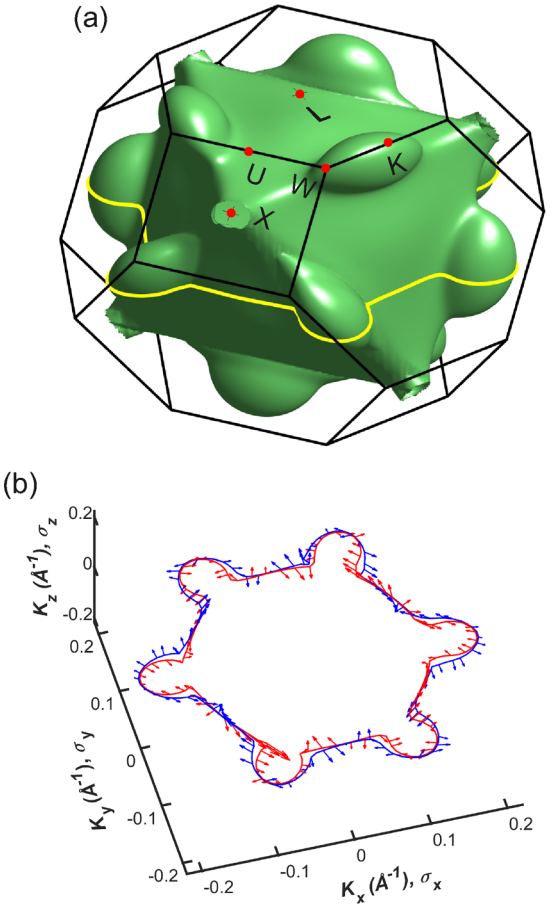

FIG. 8. RuN Fermi surface. Outer branch (a) and cross section (b). Averaged electron spin density along the cut lines is shown by arrows.

split dispersion curves along X–W line and degenerate ones along Γ–K and Γ–L lines, which produces two Fermi surface inner and outer branches. The calculated Fermi surface outer branch is shown in Fig. 8 within the Brillouin zone. The yellow-solid line on the surface in Fig. 8(a) is a cross-section line corresponding $K_z = 0$ cut plane. The Fermi surface cross section is shown in Fig. 8(b).

Electron spin density for each band and wave vector was calculated from the wave functions obtained. Spin density averaged over reciprocal unit cell is shown in Fig. 8(b) by arrows and demonstrates the opposite spin density orientation of the both Fermi surface branches.

The density of states (DOS) presented in Fig. 9 demonstrates the metallic character of the material. It is similar to the results for the cubic F43m [12] and tetragonal I42m [13] structures. Atomic orbital projected DOS curves show the main contribution of Ru atom orbitals (82%) into the DOS at Fermi energy E_F (red curve in Fig. 9).

Electron-phonon coupling parameters λ_{e-ph} and ω_{ln} [14], which define RuN superconducting state characteristics, were calculated with the use of Quantum Espresso package [15]. $36 \times 36 \times 36$ K mesh was used for self-consistent electron wave functions calculation, and $6 \times 6 \times 6$ Q mesh was used for phonon spectrum calculation. The following values were obtained: $\lambda_{e-ph} = 0.55$, $\omega_{ln} = 386$ K.

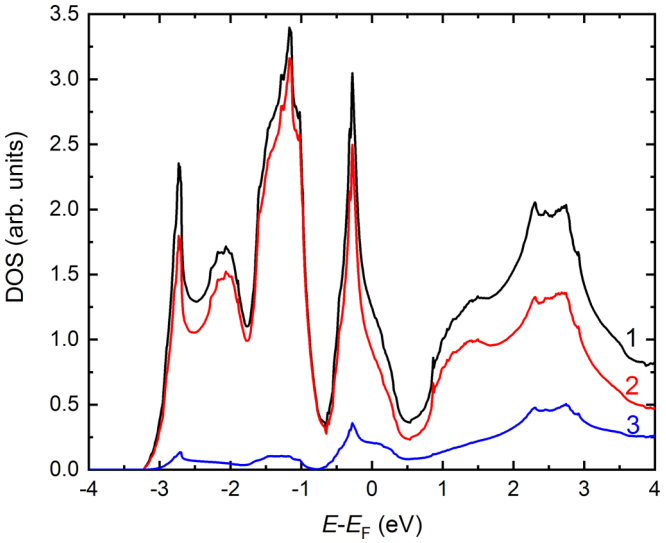

FIG. 9. RuN total density of states (black curve, 1), Ru atom orbital-projected density of states (red curve, 2), and N atom orbital-projected density of states (blue curve, 3) .

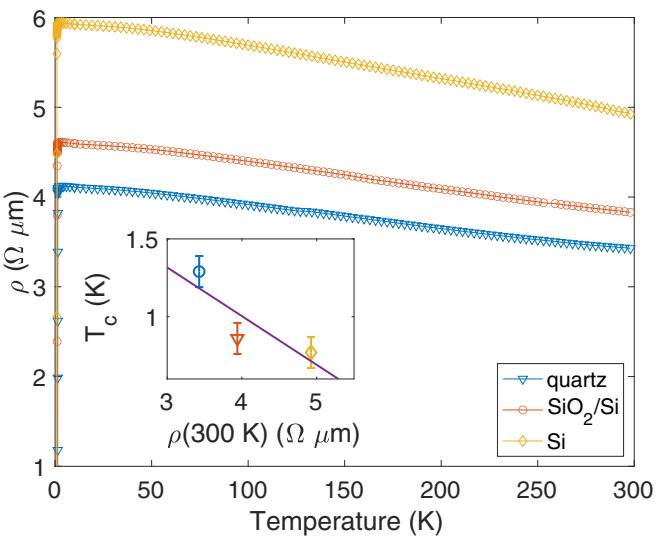

FIG. 10. Temperature dependences of resistivity of RuN films grown on different substrates in a single technological process. Film thicknesses are 105 nm (see Fig. 3). Inset shows the critical temperature vs resistivity dependence. Error bars correspond to the uncertainty associated with contact sizes. The line is a guide for the eye and corresponds to a linear root-mean-square approximation.

IV. CONDUCTING AND SUPERCONDUCTING PROPERTIES OF RuN FILMS: RESISTIVITY, UPPER CRITICAL FIELD, AND CRITICAL CURRENT

A. Sample parameters and measurement methods

Sample sizes are 8×8 mm^2 for Ru/Si film and 3.6×8 mm^2 for RuN/SiO_2 and RuN/oxidised Si films. We used soldered indium contacts for resistance measurements. Contact resistance was undetectable against the spread resistance background. The measurements were performed in the van der Pauw geometry for RuN/Si film and in the geometry with current contacts placed on the narrow ends of the substrates and potential probes attached along the wide edges of the substrates for RuN/SiO_2 and RuN/oxidized Si films. Measurements of the temperature dependences of resistance over a wide temperature range were carried out using a lock-in amplifier SRS 830 in a closed-cycle refrigerator RNA 10-320 (temperature range 10–300 K) and also in a homemade cryosystem based on a closed-circle refrigerator (temperature range 1.1–300 K). We use helium as a heat exchange gas at a pressure of 1–10 Torr. Cooling and warming rates for were around 1.5 K/min. Critical magnetic fields $H_{c2}(T)$ and critical currents were measured with a standard four-probe technique in the dilution refrigerator Bluefors BF-250LD (maximum magnetic field 1 T) in the current modulation regime using Keithley 6221 current source coupled with Keithley 2182a nanovoltmeter. When measuring $H_{c2}(T)$, magnetic field was oriented perpendicular to the films. Critical current was measured in the point contact geometry with ∼100 μm diameter indium point contact. Cooling and warming rates were around 0.005 K/min.

B. Temperature-dependent resistivity

Figure 10 shows resistivity data of RuN films. The temperature dependencies are nonmetallic ($dR/dT < 0$) for all the films, in similarity with disordered films of superconducting nitrides NbN [16]. The resistivity values are slightly different for the films and vary between 3.4 and 5.0 Ω μm, which is very close to the resistivity values of disordered NbN films [16].

C. Critical temperature and upper critical field

Figures 11 and 12 show the results of measuring the resistive transition in RuN films grown on different substrates at various values of the magnetic field. In a zero magnetic field, these films exhibit a relatively narrow resistive transition

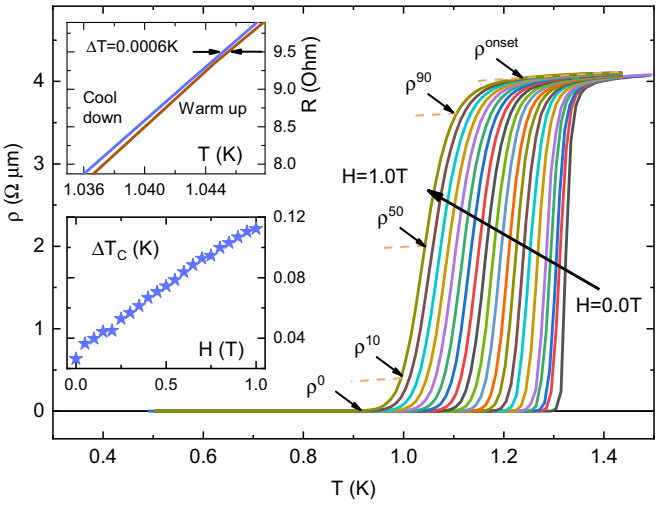

FIG. 11. Superconducting transitions in a RuN film on a polycrystalline SiO_2 substrate and their evolution with increasing magnetic field. (Top inset) An enlarged section of the resistance vs temperature curve during cooling and heating. (Bottom inset) The width of the superconducting transition as a function of the magnetic field.

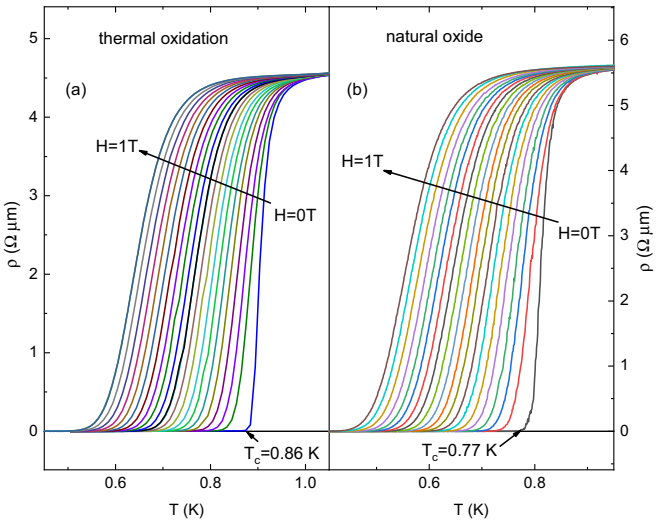

FIG. 12. Superconducting transition in RuN films on a crystalline silicon substrate with a natural oxide layer (a) and thermally oxidized surface (b) and its evolution with increasing magnetic field.

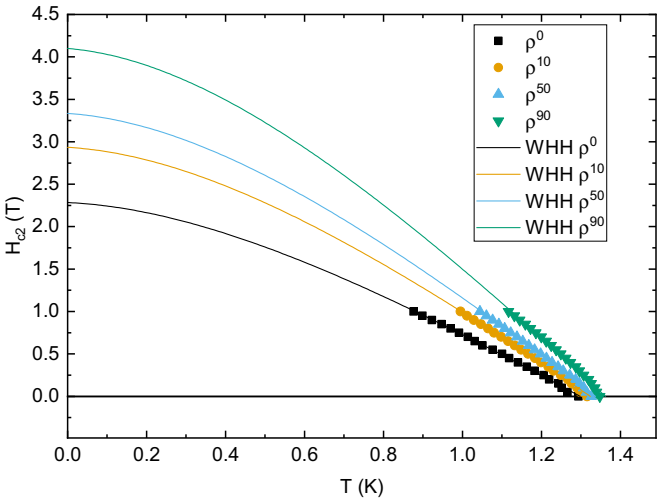

FIG. 13. Temperature dependence of the upper critical field of a RuN film on a polycrystalline SiO_2 substrate for various criteria for determining its magnitude (see text). The lines show the approximation by the WHH model [17–19] for single-zone type II superconductors.

at temperatures of 1.29 K, 0.86 K, and 0.77 K, respectively, measured at the onset of nonzero resistance. There is anticorrelation between the specific resistance at room temperature and the critical values of the films: the higher the specific resistance the lower the critical temperature (see inset in Fig. 10). The superconducting resistive transition gradually shifts to lower temperatures with an increasing magnetic field up to 1 T. It is worth noting that the width of the superconducting transition for all three samples increases significantly with increasing magnetic field, which is characteristic of hard type II superconductors, and one can expect that thermal fluctuations can play a significant role in the dissipation processes in magnetic fields.

Figure 13 shows the temperature dependencies of the upper critical magnetic field H_{c2} obtained from the curves shown in Fig. 11 measured at different values of the magnetic field. Four curves correspond to four standard criteria for determining H_{c2} (ρ^0 is zero resistance, ρ^{10} is 10% of the "value" of the superconducting transition, ρ^{50}, ρ^{90} are, respectively, 50% and 90% of the transition). An increase of the width of the superconducting transition with increasing magnetic field, which is characteristic of hard type II superconductors, is clearly seen. In the measured relatively narrow temperature range, the $H_{c2}(T)$ curves follow the WHH model [17–19]. From the results of approximation by the WHH model, the value $H_{c2}(0) = 2.3$–4.1 T for the zero-resistance criterion have been obtained.

Figure 14 shows the temperature dependencies of the upper critical field for all three samples H_{c2} obtained from the resistive transitions in Figs. 11 and 12. For clarity, we used only one criterion, r90. The inset shows the upper critical field temperature dependence in reduced coordinates: $h^* = H_{c2}(T)/(-dH_{c2}/dT)T_c$ vs $t = T/T_c$. It is clear that even though T_c and H_{c2} are strikingly different for different films, the experimentally obtained t dependence is the same at least in the temperature interval studied, in agreement with WHH model.

D. Critical current and the energy gap

The ability to carry a nondissipative current, sometimes of very high density, is one of the most valuable inherent properties of the superconductors. Not only it is an appealing attribute for practical use, but it is also a fundamental feature that provides information about the intrinsic properties of a superconductor. As was first suggested by Talantsev *et al.* [20], the temperature dependence of self-field critical current can be used to derive the energy gap and London penetration depth of superconductors. This model was successfully used to derive fundamental superconductor parameters in several dozens of materials, starting with conventional superconductors [20],

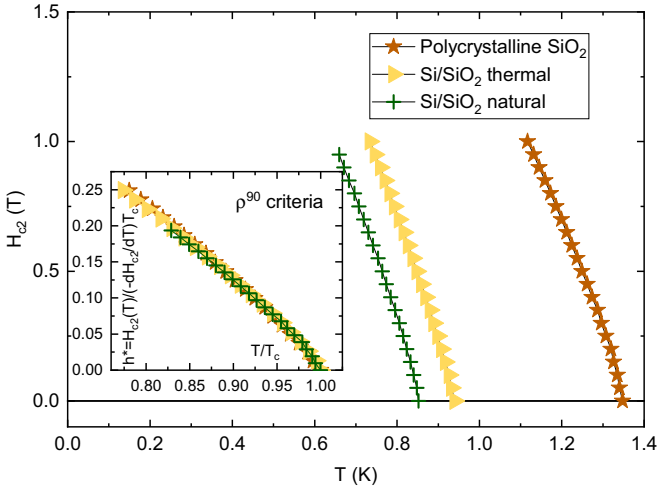

FIG. 14. Temperature dependence of the upper critical field for three different RuN films: a polycrystalline SiO_2 substrate and Si/SiO_2 substrates with thermal and natural oxidation. (Inset) Temperature dependence of a reduced critical field h^* for r90 criterion.

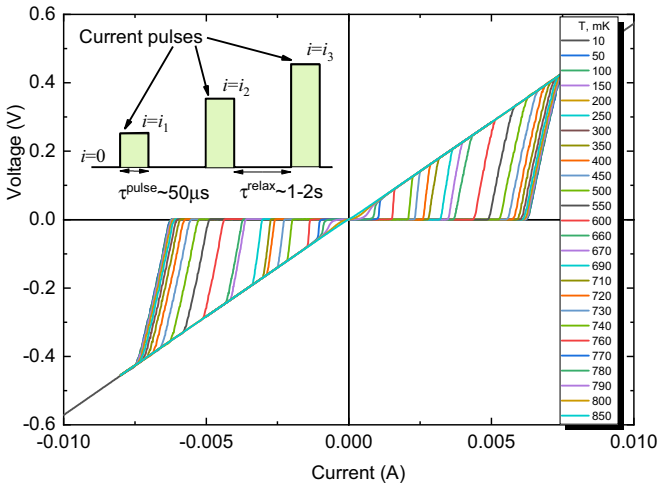

FIG. 15. Current-voltage characteristics for the RuN film on Si/SiO_2 substrate with natural oxidation in the temperature range 10–800 mK. The top left inset shows the principal scheme of the pulse measurements used for every I-V curve.

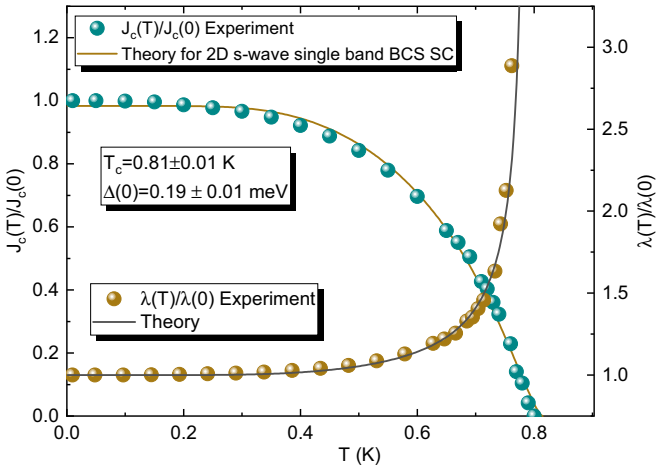

FIG. 16. Temperature dependence of the self-field critical current for RuN film on Si/SiO_2 substrate with natural oxidation ($J_0(0) = 2 \times 10^4$ A/cm^2). The dark-yellow line shows a fit by the Talantsev model for a 2D *s*-wave single band type II superconductor.

copper-based HTSC [21], iron-based HTSC [22], and even most recently discovered superhydride HTSC [23–25].

For thin films (when the half thickness of a film is smaller than the penetration depth λ), the self-field critical current density J_c^{sf} in zero external magnetic field (when the magnetic field is generated only by the current itself) is related to the penetration depth as follows [20]:

$$J_c^{sf} = \frac{\phi_0}{4\pi\mu_0\lambda^3}(\ln\kappa + 0.5) \qquad (1)$$

where ϕ_0 is flux quantum, and κ is Ginzburg-Landau parameter, which remains almost constant under the logarithm.

Since superfluid density $\rho_s \sim \lambda^{-2}$, one can determine the temperature dependence of superfluid density by measuring self-field critical current density $J_c^{sf}(T)$. Because of the practical temperature independence of $\ln(\kappa)$, for type-II superconductors, $J_c^{sf}(T)$ is dependent only on λ, which provides a tool to extract the magnitude of the superconducting gap and even its symmetry. In particular, for *s*-wave symmetry in a single-band superconductor

$$\frac{\rho_s(T)}{\rho_s(0)} = \frac{\lambda(T)^{-2}}{\lambda(0)^{-2}} = 1 - 2\sqrt{\frac{\pi\Delta(0)}{k_BT}}e^{-\Delta(0)/k_BT}. \qquad (2)$$

Thus, combining Eqs. (1) and (2), we can analyze our data within a model for a type II thin-film superconductor with *s*-wave single gap.

Figure 15 shows a set of current-voltage characteristics for RuN film on Si/SiO_2 substrate with natural oxidation. To prevent overheating the current leads, we used pulsed regime with 50 μs current pulse duration.

Figure 16 shows the temperature dependence of the self-field critical current for RuN film on Si/SiO_2 substrate with natural oxidation. The data points (blue symbols) were extracted from Fig. 15 by 0.5 mV criteria. We see that the Talantsev model [20] for 2D films with type II single gap superconductivity (light brown solid line in Fig. 16) fits the experimental data very well. The extracted energy gap value is $\Delta(0) = 0.19$ meV.

V. DISCUSSION

Epitaxial growth of RuN films shows a strong tendency (regardless of the substrate type) to grow in a single plane parallel to the substrate surface. It is well known that structures with the closest packing of a large atom (in this case Ru) in the simplest case can have either cubic or hexagonal symmetry. Cubic dense packing is three layer, and hexagonal packing is two layer. With an axial texture, crystallites rotate around an axis perpendicular to the substrate plane, so the only way to determine the type of packing is to find an asymmetric reflection and determine its interplanar distance and angle of inclination to the substrate plane. Our results indicate that the packing of layers is cubic, that is, three layer. That is, the (111) RuN plane is located parallel to the substrate plane. But its interplanar distance turns out to be greater than that of the other three planes ($\bar{1}11$). That is, the cubic structure undergoes a rhombohedral distortion, as if an elastic cube is stretched along its main diaginal line.

There are several reasons why an epitaxial layer (111) with a cubic structure undergoes rhombohedral distortion: mismatch in lattice parameters with the substrate and different thermal expansion coefficients. Since the films were forced to grow at low temperatures because of nitrogen evaporation, it is possible that nitrogen preferentially enters along the normal to the substrate. The amount of deviation of the RuN lattice angle from the right angle is too large to be caused by only one of the reasons at least in the temperature interval considered.

Instability of RuN films with respect to e-beam exposition opens very promising perspectives for e-beam profiling of the films and needs further study.

In the studied RuN films, the critical temperature of the superconducting transition temperatures ranges from 0.77 to 1.29 K, depending on the substrate. The question arises as to why films deposited in a single technological process have

such different values and other superconducting parameters. The results of the reflectometric study shown in Fig. 3 lead us to conclude that this difference results from film degradation caused by diffusion mixing of the film layer composition with the substrate. In addition, there is anticorrelation between T_c and the room-temperature resistivity of the films (see inset in Fig. 10). This anticorrelation is very similar to that observed in another superconducting nitride NbN [16], where the effect is explained by differences in the degree of disorder in NbN films. In turn, since the thermal conductivity of silicon is two orders of magnitude higher than that of quartz, there is a correlation between the thermal conductivity of the substrate (and the surface temperature during film growth) and T_c. It is very likely, therefore, that additional substrate heating during film growth could help to improve the film quality and enhance the critical temperature. Further study is required to verify this hypothesis.

Experimental T_c lies in the interval 1.29–1.4 K for RuN films on a quartz glass substrate according to Fig. 11. On the other hand, T_c can be estimated from the results of the simulation using a semi-phenomenological formula based on Eliashberg's theory [14] with calculated λ and ω_{ln} parameters. The experimental T_c interval can be obtained at the Coulomb pseudopotential values $\mu = 0.189-0.192$. In these calculations, μ is considered as a phenomenological parameter. Conventional values of μ are lying in the interval 0.1–0.15 [14], so calculated T_c overestimates somewhat measured one. Similar μ overestimation occurs in some transition metals as Nb and V [26,27]. This can be explained by neglecting some additional electron-electron correlations in T_c calculations. One possible mechanism of T_c correction is the destructive influence of the spin fluctuations [27].

The transition temperature determines the upper Pauli paramagnetic limit of H_{c2}, which has a form $H_p[\mathrm{T}] = 1.86T_c[\mathrm{K}]$ for BCS-like superconductors [28,29]. Measured T_c values correspond to $H_p = 2.4-2.6\,\mathrm{T}$. It is known [30] that the Pauli limiting term is renormalized for strong coupling superconductors $\tilde{H}_p = (1+\lambda)H_p$. $\tilde{H}_p = 3.7-4.0\,\mathrm{T}$ for the samples considered here. The maximum value of H_{c2} obtained from the experiment is equal to 4.1 T, i.e., corresponds to the maximum calculated values of $\tilde{H}_p$. It should be noted that in most typical superconductors H_{c2} is less than one half of H_p. To explain the observed anomaly, first of all we should consider a possible T_c suppression owing to the either order parameter fluctuations or sample structure related effects as the effect of the film granularity and proximity effect. The estimation of the bulk order parameter fluctuations effect is based on Ginzburg-Levanyuk criterion for dirty superconductors

$$\frac{\Delta T}{T_c} = 1.6\frac{T_c}{(k_F l)^3 E_F},$$

where ΔT is a fluctuation temperature interval in the vicinity of T_c, k_F is a Fermi wave vector and l is an electron mean free path [31]. Using $E_F \approx 3\,\mathrm{eV}$ and $k_F l \sim 1$ we get $\Delta T/T_c \approx 6\times10^{-3}$, so we can neglect the influence of these fluctuations on T_c. Both the fluctuations in granular superconductors and proximity effect in thin film should be accompanied by an upward curvature of the $H_{c2}(T)$ curve near T_c [32,33]. This upward curvature is not observed in our results. Thus, we see no supporting evidence for suppression of T_c by the fluctuation effects or film structure effects in our measurements.

The high enough value of H_{c2} can be explained by the electron spin-orbit interaction with impurities [19]. Fermi-level electrons are mostly related to Ru atomic orbitals according to the results of DOS computation (Fig. 9), and an excess Ru atom concentration over N atoms (see Sec. II B) provides spin-orbit scattering centers. Moreover, the structure of RuN has no inversion symmetry, so we cannot exclude a mixing of singlet and triplet pairing in the presence of spin-orbit interaction, which increases the upper limit of H_{c2} as well [34]. Further study is required to reveal the nature of high value of H_{c2}.

VI. CONCLUSIONS

In conclusion, we observed superconductivity in RuN films obtained by reactive magnetron sputtering on Si, oxidized Si, and silica glass substrates. The critical superconducting transition temperature ranges from 0.77 to 1.29 K depending on the substrate and is anticorrelated with the resistance of the films at room temperature. The crystal lattice is cubic with the following parameters: $a = b = c = 4.559\,\text{Å}$ for RuN/SiO_2, $a = b = c = 4.536\,\text{Å}$ for RuN/Si, and $\alpha = \beta = \gamma = 87.96^\circ$ for both films. DFT calculations, together with the results of temperature-dependent self-field critical current measurements, prove that RuN is a single-gap superconductor with $\Delta(0) = 0.19\,\mathrm{meV}$. The upper critical magnetic field $H_{c2}(0)$ was calculated by extrapolation to $T = 0$ of our data collected at $T \gtrapprox 0.8$ within the WHH model. The value of $H_{c2}(0) = 2.3$–$4.1\,\mathrm{T}$ depends on the substrate and is near the paramagnetic limit of the strong coupling case.

Data will be made available on a reasonable request.

ACKNOWLEDGMENTS

The work was supported by the Russian Science Foundation (Project No. 21-72-20114). The studies were carried out using the equipment of the Centre of Collective Usage of the Lebedev Physical Institute of RAS. The computations in this study were performed using computational resources at the Joint Supercomputer Center, Russian Academy of Science.

The authors declare that they have no known competing financial interests or personal relationships that could have appeared to influence the work reported in this paper.

[1] H. Wang, J. Li, K. Li, Y. Lin, J. Chen, L. Gao, V. Nicolosi, X. Xiao, and J.-M. Lee, Transition metal nitrides for electrochemical energy applications, Chem. Soc. Rev. **50**, 1354 (2021).

[2] M. Gurvitch, J. Remeika, J. Rowell, J. Geerk, and W. Lowe, Tunneling, resistive and structural study of NbN and other superconducting nitrides, IEEE Trans. Magn. **21**, 509 (1985).

[3] E. Gregoryanz, C. Sanloup, M. Somayazulu, J. Badro, G. Fiquet, H.-k. Mao, and R. J. Hemley, Synthesis and characterization of a binary noble metal nitride, Nat. Mater. **3**, 294 (2004).

[4] M. Moreno-Armenta, J. Diaz, A. Martinez-Ruiz, and G. Soto, Synthesis of cubic ruthenium nitride by reactive pulsed laser ablation, J. Phys. Chem. Solids **68**, 1989 (2007).

[5] Y.-H. Liao and J.-C. Chou, Fabrication and characterization of a ruthenium nitride membrane for electrochemical pH sensors, Sensors **9**, 2478 (2009).

[6] C.-Y. Wu, W.-H. Lee, S.-C. Chang, Y.-L. Cheng, and Y.-L. Wang, Effect of annealing on the microstructure and electrical property of RuN thin films, J. Electrochem. Soc. **158**, H338 (2011).

[7] S. Bouhtiyya, R. Lucio Porto, B. Laïk, P. Boulet, F. Capon, J. Pereira-Ramos, T. Brousse, and J. Pierson, Application of sputtered ruthenium nitride thin films as electrode material for energy-storage devices, Scr. Mater. **68**, 659 (2013).

[8] E. Cattaruzza, G. Battaglin, P. Riello, D. Cristofori, and M. Tamisari, On the synthesis of a compound with positive enthalpy of formation: Zinc-blende-like RuN thin films obtained by rf-magnetron sputtering, Appl. Surf. Sci. **320**, 863 (2014).

[9] E. Cattaruzza, G. Battaglin, D. Cristofori, T. Finotto, P. Riello, and A. Glisenti, On the synthesis and thermal stability of RuN, an uncommon nitride, Surf. Coat. Technol. **295**, 93 (2016).

[10] X. Gonze, B. Amadon, G. Antonius, F. Arnardi, L. Baguet, J.-M. Beuken, J. Bieder, F. Bottin, J. Bouchet, E. Bousquet *et al.*, The ABINIT project: Impact, environment and recent developments, Comput. Phys. Commun. **248**, 107042 (2020).

[11] L. P. R. René de Cotret, M. R. Otto, M. J. Stern, and B. J. Siwick, An open-source software ecosystem for the interactive exploration of ultrafast electron scattering data, Adv. Struct. Chem. Imaging **4**, 2198 (2018).

[12] W. Chen and J. Jiang, Elastic properties and electronic structures of 4d- and 5d-transition metal mononitrides, J. Alloys Compd. **499**, 243 (2010).

[13] Y. Zhang, L. Wu, and B. Wan, Diverse ruthenium nitrides stabilized under pressure: a theoretical prediction, Sci. Rep. **6**, 33506 (2016).

[14] P. B. Allen and R. C. Dynes, Transition temperature of strong-coupled superconductors reanalyzed, Phys. Rev. B **12**, 905 (1975).

[15] P. Giannozzi, S. Baroni, and N. Bonini, QUANTUM ESPRESSO: a modular and open-source software project for quantum simulations of materials, J. Phys.: Condens. Matter **21**, 395502 (2009).

[16] M. Chand, A. Mishra, Y. M. Xiong, A. Kamlapure, S. P. Chockalingam, J. Jesudasan, V. Bagwe, M. Mondal, P. W. Adams, V. Tripathi, and P. Raychaudhuri, Temperature dependence of resistivity and Hall coefficient in strongly disordered NbN thin films, Phys. Rev. B **80**, 134514 (2009).

[17] E. Helfand and N. R. Werthamer, Temperature and purity dependence of the superconducting critical field, H_{c2}, Phys. Rev. Lett. **13**, 686 (1964).

[18] E. Helfand and N. R. Werthamer, Temperature and purity dependence of the superconducting critical field, H_{c2}. II, Phys. Rev. **147**, 288 (1966).

[19] N. R. Werthamer, E. Helfand, and P. C. Hohenberg, Temperature and purity dependence of the superconducting critical field, H_{c2}. III. Electron spin and spin-orbit effects, Phys. Rev. **147**, 295 (1966).

[20] E. F. Talantsev and J. L. Tallon, Universal self-field critical current for thin-film superconductors, Nat. Commun. **6**, 7820 (2015).

[21] E. Talantsev, W. P. Crump, and J. L. Tallon, Thermodynamic parameters of single-or multi-band superconductors derived from self-field critical currents, Ann. Phys. (Leipzig) **529**, 1700197 (2017).

[22] E. Talantsev, K. Iida, T. Ohmura, T. Matsumoto, W. Crump, N. Strickland, S. Wimbush, and H. Ikuta, *p*-wave superconductivity in iron-based superconductors, Sci. Rep. **9**, 14245 (2019).

[23] E. F. Talantsev, W. P. Crump, J. G. Storey, and J. L. Tallon, London penetration depth and thermal fluctuations in the sulphur hydride 203 K superconductor, Ann. Phys. (Leipzig) **529**, 1600390 (2017).

[24] I. A. Troyan, D. V. Semenok, A. G. Ivanova, A. V. Sadakov, D. Zhou, A. G. Kvashnin, I. A. Kruglov, O. A. Sobolevskiy, M. V. Lyubutina, T. Helm *et al.*, Non-Fermi-liquid behavior of superconducting snh_4, Adv. Sci. **10** 2303622 (2023).

[25] A. V. Sadakov, V. A. Vlasenko, I. A. Troyan, O. A. Sobolevskiy, D. V. Semenok, D. Zhou, and V. M. Pudalov, Vortex phase dynamics in yttrium superhydride YH_6 at megabar pressures, J. Phys. Chem. Lett. **14**, 6666 (2023).

[26] E. Drzazga, I. Domagalska, M. Jarosik, R. Szcześniak, and J. Kalaga, Characteristics of superconducting state in vanadium: The Eliashberg equations and semi-analytical formulas, J. Supercond. Nov. Magn. **31**, 1029 (2018).

[27] H. Rietschel and H. Winter, Role of spin fluctuations in the superconductors Nb and V, Phys. Rev. Lett. **43**, 1256 (1979).

[28] A. M. Clogston, Upper limit for the critical field in hard superconductors, Phys. Rev. Lett. **9**, 266 (1962).

[29] B. S. Chandrasekhar, A note on the maximum critical field of high-field superconductors, Appl. Phys. Lett. **1**, 7 (1962).

[30] M. Schossmann and J. P. Carbotte, Pauli limiting of the upper critical magnetic field, Phys. Rev. B **39**, 4210 (1989).

[31] A. Larkin and A. Varlamov, *Theory of Fluctuations in Superconductors* (Oxford University Press, Oxford, 2005), Vol. 127.

[32] G. Deutscher, O. Entin-Wohlman, and Y. Shapira, Upper critical fields in granular superconductors, Phys. Rev. B **22**, 4264 (1980).

[33] A. S. Sidorenko, C. Sürgers, and H. Löhneysen, Perpendicular upper critical field of a proximity-coupled superconducting film, Physica C: Supercond. **370**, 197 (2002).

[34] M. Smidman, M. B. Salamon, H. Q. Yuan, and D. F. Agterberg, Superconductivity and spin-orbit coupling in non-centrosymmetric materials: a review, Rep. Prog. Phys. **80**, 036501 (2017).